



Article

Self-Oscillating Converter Based on Phase Tracking Closed Loop for a Dynamic IPT System

Lin Chen ¹, Daqing Luo ², Jianfeng Hong ^{3,*}, Mingjie Guan ²  and Wenxiang Chen ^{2,*} ¹ Xiamen Kehua Digital Energy Tech Co., Ltd., Xiamen 361000, China; khchenlin@kehua.com² Department of Instrumental and Electrical Engineering, Xiamen University, Xiamen 361005, China; 35120191151194@stu.xmu.edu.cn (D.L.); mjguan@xmu.edu.cn (M.G.)³ School of Automotive and Mechanical Engineering, Xiamen University of Technology, Xiamen 361005, China

* Correspondence: 2020000040@xmut.edu.cn (J.H.); wxchen@xmu.edu.cn (W.C.)

Abstract: The coupling of converters with resonant networks poses significant challenges for frequency tracking and power control in inductive power transfer (IPT) systems. This paper presents an implementation method that addresses these issues by dividing the system's operation into two distinct states: self-oscillating and power-injecting. Based on these states, a phase-closed loop is constructed. Within this closed loop, the phase tracking unit detects and tracks frequency drift, while the power regulating unit incorporates an integrator and adopts a control variable to adjust the output power by modifying the duration of the power injecting state. Meanwhile, the oscillating unit operates in the self-oscillating state. Operating in this manner, the system achieves self-oscillation and demonstrates the capability to effectively track and compensate for system variations within a single cycle. A verification prototype has been constructed, and it demonstrates that the converter within it completely decoupled from the resonant network. Experimental results validate that altering the control variable solely affects the duration of the power-injecting state, allowing for independent control of the output power. When the control variable changes from 2.0 V to 3.5 V, the output power changes from 178 W to 519 W while the self-oscillating state remains unchanged. Furthermore, the system accurately tracks frequency changes, even under significant variations in the coupling coefficient or load, without compromising the power injection state. When the air gap changes from 3 cm to 12 cm, the duration of the self-oscillating state changes from 22.1 μ s to 26.3 μ s, while the power injecting state remains unchanged. This approach exhibits a robust performance, particularly suitable for dynamic IPT systems sensitive to parameter variations.

Keywords: dynamic system; inductive power transfer; phase-closed loop; self-oscillating



Citation: Chen, L.; Luo, D.; Hong, J.; Guan, M.; Chen, W. Self-Oscillating Converter Based on Phase Tracking Closed Loop for a Dynamic IPT System. *Energies* **2024**, *17*, 1814. <https://doi.org/10.3390/en17081814>

Academic Editor: Mario Marchesoni

Received: 2 March 2024

Revised: 3 April 2024

Accepted: 5 April 2024

Published: 10 April 2024



Copyright: © 2024 by the authors. Licensee MDPI, Basel, Switzerland. This article is an open access article distributed under the terms and conditions of the Creative Commons Attribution (CC BY) license (<https://creativecommons.org/licenses/by/4.0/>).

1. Introduction

Inductive power transfer (IPT) is a technology that enables power transmission through a magnetic flux without physical contact. It has found widespread applications in various fields, including electric vehicles, mobile phones, and medical transplantation [1–3]. However, IPT systems are classified as loosely coupled systems compared to tightly coupled systems. In an IPT system, the primary and secondary coils form a loosely coupled transformer, resulting in poor magnetic coupling between the two sides. This leads to power reduction, decreased efficiency, and increased VA capacity of the converter.

To address this issue, extensive research has been conducted. Mainstream solutions involve incorporating a resonant network (compensation network) into a series between the converter and primary circuit, as well as the secondary circuits and load circuit [3–5]. The resonant network primarily consists of reactive elements, with capacitors being the main component. Resonant networks are categorized into nine basic types based on the series or parallel connection of capacitors [6], with four (S-S, S-P, P-S and P-P) being extensively studied and considered to be mainstream topologies [7–9].

However, the introduction of a resonant network in an IPT system introduces coupling and mutual interference between the converter and the resonant network during operation. To ensure the stability of the IPT system, it is necessary for the converter frequency to align with the resonant network frequency, thus ensuring a zero phase angle impedance (ZPA) in the primary circuit [10]. Additionally, IPT systems experience the problem of frequency bifurcation [11]. Due to the possibility of misalignment, an uncertainty between the loosely coupled transformer and resonant network occurs, which leads to frequency shifts and bifurcation [12,13], therefore, frequency tracking is necessary.

One common approach is to insert a controlled impedance network on the primary and secondary sides to match any changes that may occur [14–17]. These controllable impedance networks typically employ self-switching reactive elements, such as self-switching capacitors [1,14]. However, this tracking method has a disadvantage in that it cannot cover the entire frequency range due to the limited number of switches available. Another approach is to utilize a phase-locked loop (PLL) to construct a frequency loop for accurate frequency tracking [18–20]. However, the drawback of PLL is that it introduces circuit complexity and may have tracking delay.

The self-oscillating technique is widely employed in various applications, including induction heating, and has also been used in IPT system. This technique utilizes a sensor and sampling circuit to track the zero crossing of the primary current. The switches are then triggered at the zero crossing point to generate self-excited oscillation. By employing this method, the converter and resonant network frequencies can be synchronized, ensuring accurate frequency tracking [21–25]. Nevertheless, in these self-oscillation applications, it is crucial for the converter frequency to align with the resonant network frequency. Consequently, some coupling between the converter and the resonant network still exists, requiring the operation of switches at the zero crossing point. This, in turn, amplifies the complexity of the control strategy. Furthermore, due to the inherent delay introduced by the sensor, sampling and shaping circuits, the actual switching point may deviate from the zero crossing, resulting in the loss of soft switching opportunities.

In practice applications, it is necessary to regulate the voltage and power to achieve the desired output. Conventional solutions involve using a DC/DC converter in either the primary or secondary sides to control the bus voltage and load impedance [26,27] or regulating phase shift to control power flow [28,29]. However, inserting a DC/DC converter into the system introduces additional losses, which can result in decreased overall efficiency. On the other hand, the phase-shifting technology may cause the switching point to deviate from the zero crossing, leading to the loss of the soft switching condition.

In the literature [30,31], a quasi-resonant control strategy is presented that divides an energy transfer period into two states: the resonant state and the energy-independent injection state. This control strategy provides an effective scheme for power control. During the resonant state, the converter is isolated from the resonant network, allowing the system to resonate freely. This resonant state lasts for less than one cycle, enabling frequency tracking during this period. In the energy injection state, the resonant network is isolated from the converter, and the power source directly injects energy into the primary inductor. This decouples the converter from the resonant network, allowing for the independent regulation of power by adjusting the duration of the energy injection state. The limitation of the literature [30,31] lies in the complexity of the system control strategy and the absence of a closed-loop scheme.

In this paper, the objective is to find a way to eliminate the coupling between the converter and the resonant network, allowing them to operate independently, and reducing the problems caused by coupling. To accomplish this, this paper proposes a variable structure approach that divides a converter into three fundamental operating states: switch-on state, blocking state, and diode-on state, based on their functions within an IPT system.

In these three states, the blocking state serves to achieve quasi-resonance within the system and is employed for tracking changes in system frequency. The switch-on state is utilized to inject power and adjust the output power. The diode state maintains

soft switching conditions for the converter when transitioning between the blocked and switched states.

Furthermore, these three states can be combined into two distinct states: quasi-resonant and power injection states, which are independent of each other.

Building upon this foundation, this paper introduces a phase-closed loop control topology based on the quasi-resonant and power injection modes. In this closed-loop system, the phase of the quasi-resonant state acts as a feedback signal, triggering the self-oscillation of the system. This means that the system can achieve self-sustained oscillation without the need for external control. Additionally, within this closed-loop, a control variable is employed to regulate the duration of the power injection mode for power adjustment. To facilitate clear understanding, we refer to the quasi-resonant state as the self-oscillating state, while the power injection state retains its original designation.

For a better understanding, Table 1 briefly compares the coupling between existing converters and resonant networks, as well as the power regulation techniques.

Table 1. The comparison of the decoupling ability and power regulation effect between this work and the literature.

Ref.	Compensation Network	Closed-Loop	Feedback Signal	Resonant Mode	Coupling between Converter and Network	Power Control Strategy
[20]	S-S	Yes	Primary side Current	Perfect resonance	Strong	—
[23]	S-S	Yes	Primary side Current	Perfect resonance	Strong	Regulating phase
[25]	S-CC	Yes	Current from current transformer	Perfect resonance	Strong	Regulating phase
[26]	S-S	Yes	Load voltage	Perfect resonance	Strong	Additional converter
[28]	LCC-S	Yes	Load voltage and current	Perfect resonance	Strong	Regulating phase
[31]	P-S	No	—	quasi-resonant	No	Regulating the duration of energy injection state
This work	P-P	Yes	Voltage from primary side	quasi-resonant	No	Regulating the duration of energy injection state

Adopting a closed-loop control strategy in prior studies has essentially solved the problem of frequency tracking. However, the coupling between the converter and the resonant network persists, requiring switching points at current zero crossings, which complicates system control. Additionally, power regulation in prior studies still relies on techniques like phase shifting or adding DC/DC converters, whose drawbacks have been discussed extensively in much of the literature.

In document [31], a strategy of time-sharing energy injection and free resonance is adopted based on the quasi-resonant mode to address the coupling and power regulation issues. However, it falls short in establishing closed-loop control and providing a comprehensive solution.

To address these shortcomings, this paper proposes dividing the converter's operation into three modes: blocking, diode conduction, and switch conduction. These modes allow for dividing the energy transmission period into two states: free resonance and power injection. This approach achieves decoupling between the converter and the resonant network

and enables power adjustment by controlling the energy injection time. With closed-loop control, it exhibits favorable dynamic characteristics and power adjustment capabilities.

2. Variable Structure Analysis of an IPT System

Figure 1a depicts an IPT charging system with a converter in the primary side and a resonant network (compensation network) on both the primary and secondary sides. In Figure 1a, the U_{DC} represents the DC source that supplies power to the system, and R_L stands for load. C_p and L_p constitute the primary resonant network, while C_s and L_s constitute the secondary resonant network. Mutual inductance, M , establishes a magnetic link between the primary and the secondary to transmit power. Furthermore, L_p and L_s together form a loosely coupled transformer. It is evident that this IPT system belongs to P-P compensation topology.

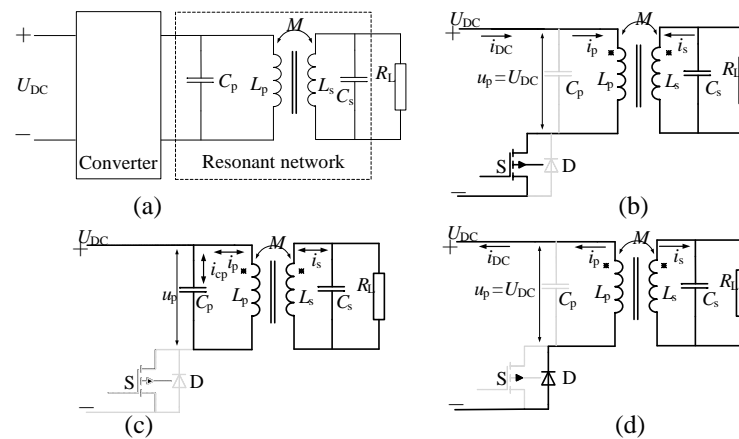


Figure 1. (a) An IPT system using P-P compensation network. (b) The IPT system that the converter is in the switch-on state. (c) The IPT system that the converter is in the blocking state. (d) The IPT system that the converter is in the diode-on state.

It is widely recognized that the converter can be constructed using various topologies such as full-bridge, half-bridge, or single switch configurations. These topologies employ semiconductor switches, with each switch being equipped with a body diode. Consequently, during the operation of an IPT system, the converter can be categorized into three states based on its working structure: the switch-on state, the blocking state, and the diode-on state.

To visually illustrate these three states, Figure 1b–d employ a single switch converter as an example. In this context, S represents a semiconductor device, such as an IGBT, while D signifies the body diode associated with S .

Figure 1b illustrates the behavior of the switch-on state of a converter. During this state, the switch S is activated to deliver U_{DC} to L_p , generating a primary inductor current i_p with the slope of K_E , injecting power into the system, and the value of K_E can be determined as follows:

$$K_E = \frac{U_{DC}}{L_p} \quad (1)$$

In the switch-on state, due to the connection of U_{DC} to L_p , the voltage across C_p is clamped at U_{DC} , and there is current flowing into the secondary coil.

Figure 1c depicts the behavior of the blocking state, where both switches and diodes are deactivated, leading to the isolation of U_{DC} from the resonant network. During this state, the resonant network initiates oscillation with an angular frequency ω . This angular frequency is solely determined by the system parameters, such as C_p , L_p and secondary reflected impedance, as the resonant network is no longer influenced by the converter.

It is important to note that C_p is connected in parallel with the output of the converter, ensuring that the voltage across C_p does not exceed U_{DC} . As a result, the oscillation of the system in the blocking state is incomplete.

Figure 1d illustrates the behavior of the diode-on state. In this state, the diode D is activated, allowing U_{DC} to be reconnected to L_p . These activated diodes provide a pathway for the current i_p to flow back to U_{DC} . Similar to the switch-on state, the voltage across C_p remains clamped at U_{DC} during the diode-on state.

While we employ a single-switch converter in the analysis of these three states, in fact, it is worth noting that these three states are also applicable to the half-bridge and full-bridge converter mentioned earlier.

If the loosely coupled transform in Figure 1 is replaced by the T model, the resonant network can be represented by the equivalent circuit shown in Figure 2. In this circuit, L_{pk} and L_{sk} denote the leakage inductances of the primary and secondary, respectively, while L_M represents the mutual inductance. The relationship between these parameters can be expressed as follows:

$$\begin{cases} L_M = M \\ L_{pk} = L_p - M \\ L_{sk} = L_s - M \\ k = \frac{M}{\sqrt{L_p L_s}} \end{cases} \quad (2)$$

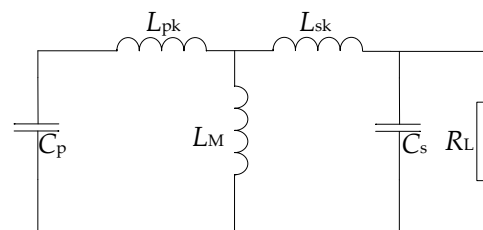


Figure 2. T equivalent model of loosely coupled transformer.

In Equation (2), k represents the coupling coefficient, which indicates the efficiency of energy transferring from the primary to secondary side. For an IPT system, the coupling coefficient k is typically weak. As a result, only a portion of the power can be transmitted to the secondary side, and a significant amount of energy remains stored in leakage inductance L_{pk} . This energy needs to be returned to U_{DC} during a power transfer period.

Based on the characteristics of the resonant network in Figure 2, the operational reality can be described as follows: during the switching on state, U_{DC} injects power into the primary inductor L_p ; during the blocking state, the injected power excites the resonant network, causing it to oscillate; and during the diode-on state, the residual energy stored in leakage inductance L_{pk} is returned to U_{DC} .

In Figure 2, capacitor C_p , inductors L_{pk} , and L_M form a compensation topology. In this compensation network, the power injected into the mutual inductance L_M is transmitted to the secondary side. Meanwhile, the power remaining in leakage inductance L_{pk} is utilized to sustain the diode-on state and subsequently returned to the power source U_{DC} .

A characteristic of the compensation network is its ability to harness the energy stored in the leakage inductance to sustain the diode-on state. This bestows a substantial soft-switching margin upon the converter. Consequently, the diode-on state can be employed to establish an isolated transition zone between the blocking state and the switch-on state. Moreover, by designing a repeating converter operational cycle as follows: blocking state \rightarrow diode-on state \rightarrow switch-on state \rightarrow blocking state, and by using some hardware circuits, we can construct a self-oscillating closed loop for an IPT system, as shown in Figure 3. With the diode-on state acting as a buffer, the system designed by this method has a wide soft switching margin.

In this self-oscillating loop, the blocking state facilitates free oscillation, the switch-on state implements power injection, and the diode-on state contributes to the soft switch behavior. By employing this approach, the decoupling between the converter and the resonant network can be achieved while also realizing self-oscillation of the system.

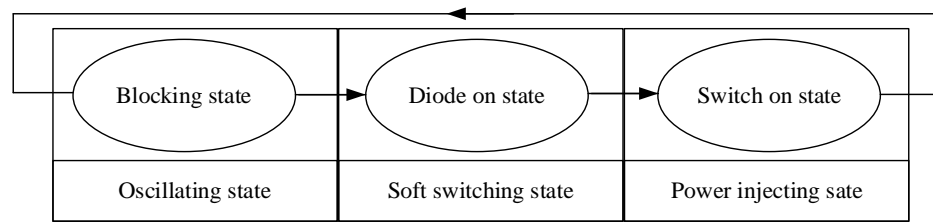


Figure 3. The states repeating order in a power transfer period.

Figure 4 provides a vector trajectory diagram and curves of this self-oscillating loop, demonstrating the dynamic behavior of i_p , u_p . To illustrate the relationship between the switch S and i_p , u_p , the control signal of S, v_g , is also depicted in Figure 4.

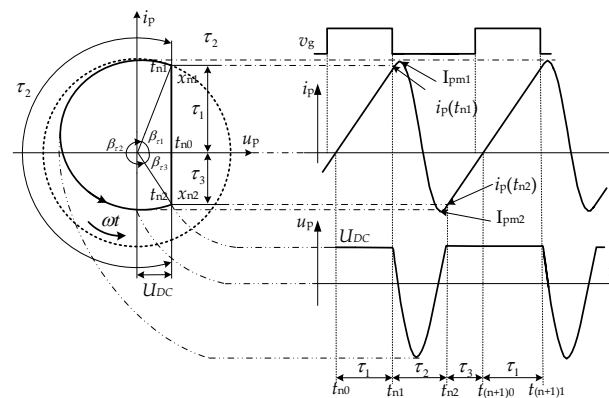


Figure 4. The vector trajectory diagram and curves of i_p , u_p .

In Figure 4, the left side displays the vector trajectory diagram. The dotted circle represents the oscillating vector trajectory, while the solid black line represents the actual running vector trajectory of i_p , u_p . Assuming that the system has achieved stability in the n th period, it can be seen that the vector trajectory forms a closed curve divided into three segments: τ_1 , τ_2 , and τ_3 , respectively. t_{n0} denotes the starting point of the switch-on state, t_{n1} is the starting point of blocking state, and t_{n2} is the starting point of the diode-on state.

Referring to Figures 1 and 4, during the τ_1 segment, $[t_{n0}, t_{n1}]$, the vector trajectory is in the switch-on state, with u_p clamped at U_{DC} . As a result, the vector trajectory in this segment is a straight line parallel to the i_p axis, where $u_p = U_{DC}$. It starts from $i_p = 0$ and extends to the oscillating circle at t_{n1} . The phase angle occupied by τ_1 is represented by $\beta_{\tau1}$.

During the τ_2 segment, $[t_{n1}, t_{n2}]$, the system enters the blocking state, and the oscillation begins. However, due to attenuation, the vector trajectory deviates from the oscillating circle and follows a decaying circular curve. The phase angle occupied by τ_2 is represented by $\beta_{\tau2}$.

During the τ_3 segment, $[t_{n2}, t_{(n+1)0}]$, the system is in the diode-on state, similar to τ_1 , with u_p clamped at U_{DC} . Consequently, the vector trajectory in this segment appears as a parallel line parallel to axis i_p , where $u_p = U_{DC}$. The phase angle occupied by τ_3 is represented by $\beta_{\tau3}$.

In Figure 4, the right side presents the curves of i_p , u_p , and the relationship between vector trajectory and these curves is indicated by dot-dash lines. Referring to Figure 1, the following is an analysis of i_p , u_p curves in different states:

$[t_{n0}, t_{n1}]$: This interval represents the switch-on state, τ_1 . The control signal v_g has been at a high level, indicating that switch S has been turned on and U_{DC} supplied to L_p . The current i_p increases linearly from zero with slope K_E , while u_p remains clamped at U_{DC} . At t_{n1} , when i_p reaches $i_p(t_{n1})$, v_g is pulled to a low level, turning off switch S, and the system exits the switch-on state. As the voltage of C_p is equal to U_{DC} , switch S is turned off with the zero voltage switch (ZVS) condition.

$[t_{n1}, t_{n2}]$: This interval represents the blocking state. During this interval, the system experiences oscillation at the angular frequency ω , causing in-sinusoidal variations in both

u_p and i_p . Since the phase angle occupied by oscillation segment, $\beta_{\tau 2}$, is greater than π but less than 2π , the i_p exhibits two amplitudes, I_{pm1} , I_{pm2} , within this interval. Between these two amplitudes, i_p passes through a zero crossing.

After t_{n1} , the capacitor voltage u_p starts to decrease from its maximum value, U_{DC} . It then reaches its lowest point at the zero crossing of the current, i_p . Subsequently, as u_p begins to rise again, it reaches U_{DC} once more at t_{n2} . When u_p reaches U_{DC} , diode D is turned on, clamping u_p to U_{DC} again. Consequently, the system loses the oscillation condition and exit the blocking state at t_{n2} . At t_{n2} , the current i_p reaches value of $i_p(t_{n2})$.

$[t_{n2}, t_{(n+1)0}]$: This interval represents the diode-on state. After t_{n2} , the current i_p increase linearly from $i_p(t_{n2})$ with a slope of k_E , indicating that the energy stored in the leakage inductor L_{pk} flows back to power source during this interval. Assuming that the switch S has been turned on before i_p reaches its zero crossing, as shown in Figure 4, the system will automatically transition from the diode-on state to the switch-on state at the zero crossing of i_p , denoted as point $t_{(n+1)0}$. Therefore, after $t_{(n+1)0}$, the system will exit from the diode-on state and enter the switch-on state again, initiating a new power injection process.

Although the converter mentioned above is divided into three states, Figure 4 shows that the vector trajectories of the switch-on state and the diode-on state are the same line segment parallel to i_p axis. Additionally, as depicted in Figure 1, in both states, U_{DC} is directly connected to L_p , and the voltage of C_p is clamped at U_{DC} . That is to say, the function of both states is to maintain the power flow in or out of L_p . Therefore, these two states can be collectively referred to as power injecting states, and the durations τ_1 and τ_3 can be combined into $\tau_{inj} = \tau_1 + \tau_3$. Similarly, the blocking state can also be referred to as a self-oscillating state, and the duration τ_2 can be denoted as τ_{osc} .

The value of τ_{osc} depends on the phase angle $\beta_{\tau 2}$ and the angular frequency ω , which are determined by real-time parameters. Therefore, frequency tracking can be achieved by monitoring τ_{osc} and implementing appropriate compensation. On the other hand, the power injected from U_{DC} to L_p is determined by the duration of power injection state, τ_{inj} . That is to say, τ_{inj} can be used as a control variable to regulate the system power.

Figure 5 is utilized to illustrate the impact of parameter changes on τ_{osc} and τ_{inj} during the operation of the proposed IPT system. When parameters are modified, the system follows a new vector trajectory, resulting in corresponding alterations in the curves of i_p , u_p . In Figure 5, the trajectories and curves with unchanged parameters are represented in green, while those after the changes are depicted in red. By comparing the green and red voltage curve, it can be observed that changes in system parameters result in a shift in the start time of the oscillation state from t_{n1} to t_{n1}' , a shift in the end time from t_{n2} to t_{n2}' , a change in the angular frequency from ω to ω' and a change in the phase angle from $\beta_{\tau 2}$ to $\beta_{\tau 2}'$. These changes cause a shift in the duration of the oscillating state from τ_{osc} to τ_{osc}' .

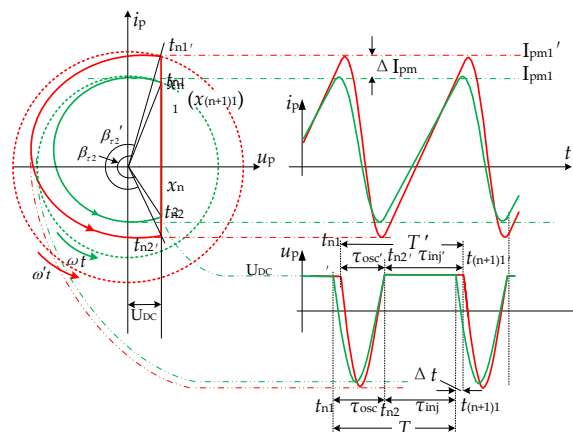


Figure 5. Effect of the system parameters on τ_{osc} and τ_{inj} .

3. Mathematical Model

Figure 6 illustrates a schematic diagram of the power injecting model.

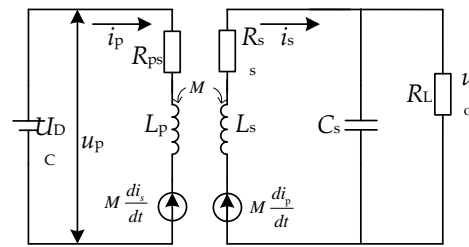


Figure 6. Power injecting model. Here, i_p , i_s represent the primary and secondary current, and u_p signifies the primary capacitor voltage.

On the primary side, the U_{DC} directly supplies to L_p . Taking into account the copper resistance of the coil, R_{ps} and R_{ss} denote the loss resistances of the primary and secondary inductors, respectively. L_p and L_s act as power transfer channels, creating a loosely coupled transformer between the primary and secondary sides. The symbol M represents the mutual inductance of the transformer. Additionally, the controlled voltage $M \times di_p/dt$ signifies the impact of the secondary current on the primary side, while $M \times di_s/dt$ represents the effect of the primary current on the secondary side.

Figure 7 depicts the schematic diagram of the oscillating state model. In this model, the power source U_{DC} illustrated in Figure 6 is replaced with the capacitor C_p , while the remaining components remain unchanged as depicted in Figure 6.

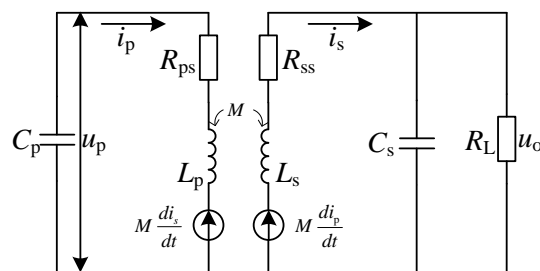


Figure 7. Oscillating model. Here, i_p , i_s represent the primary and secondary current, and u_p signifies the primary capacitor voltage.

If a power electronic system exhibits multiple structures periodically during each stabilization period, these structures are determined by the actual state of the circuit. Meanwhile, these structures possess their own linear dynamics, and the system can be modeled using a general state space representation [32]:

$$\begin{cases} x' = A_i x + B_i u & i = \text{osc, inj} \\ y = Cx \end{cases} \quad (3)$$

where, A is the characteristic matrix, B is the input matrix, C is the output matrix and i represents the serial number of each structures. Respectively, x represents the state variable, with $x = [u_p, i_p, i_s, u_o]^T$; u denotes the input variable, with $u = [U_{DC}]$; and y represents the output variable.

Based on Figures 6 and 7, the characteristic matrix and input matrix of the power-injecting and self-oscillating states can be written as Equations (4) and (5).

$$A_{inj} = \begin{bmatrix} -1 & 0 & 0 & 0 \\ 0 & -\frac{L_s R_{ps}}{\Delta} & -\frac{M R_{ss}}{\Delta} & -\frac{M}{\Delta} \\ 0 & -\frac{M R_{ps}}{\Delta} & -\frac{L_p R_{ss}}{\Delta} & -\frac{L_p}{\Delta} \\ 0 & 0 & \frac{1}{C_s} & -\frac{1}{C_s R_L} \end{bmatrix} \quad (4)$$

$$B_{inj} = \begin{bmatrix} 1 & \frac{L_s}{\Delta} & \frac{M}{\Delta} & 0 \end{bmatrix}^T$$

$$A_{osc} = \begin{bmatrix} 0 & -\frac{1}{C_p} & 0 & 0 \\ \frac{L_s}{\Delta} & -\frac{L_s R_{ps}}{\Delta} & -\frac{M R_{ss}}{\Delta} & -\frac{M}{\Delta} \\ \frac{M}{\Delta} & -\frac{M R_{ps}}{\Delta} & -\frac{L_p R_{ss}}{\Delta} & -\frac{L_p}{\Delta} \\ 0 & 0 & \frac{1}{C_s} & -\frac{1}{C_s R_L} \end{bmatrix} \quad (5)$$

$$B_{osc} = \begin{bmatrix} 0 & 0 & 0 & 0 \end{bmatrix}^T$$

In the time domain, when the variable t is used as the time variable for each state running process, then, the solution of Equation (3) represents the time function that describes the system behavior [33]:

$$x(t) = \Phi_i(t - t_0)x_0 + A_i^{-1}(\Phi_i(t - t_0) - I)B_i u \quad i = osc, inj \quad (6)$$

where, x_0 represents the initial value at the beginning of each state at time t_0 , with $x_0 = x(t_0)$. I denotes the identity matrix. $\Phi(t)$ is defined as $\Phi(t) = \exp\{A_i t\}$, $i = inj, osc$.

Referring back to Figure 5 to discuss the contents of the green line, in the proposed IPT system, as described earlier, there exist two states durations, namely τ_{osc} and τ_{inj} , respectively. Therefore, as depicted in Figure 5, a power transfer period T can be defined as follows:

$$T = \tau_{osc} + \tau_{inj} \quad (7)$$

Let us begin by analyzing the interval $[t_{n1}, t_{n2}]$, which represents the oscillating state duration. According to Equation (5), in this interval, the input matrix B is a zero matrix. Therefore, Equation (6) can be rewritten as follows:

$$x(t) = \Phi_{osc}(t - t_{n1})x_{n1} \quad t_{n1} \leq t < t_{n2} \quad (8)$$

Then, let us analyze the interval $[t_{n2}, t_{(n+1)1}]$, which represents the power injecting state duration. According to Equation (4), Equation (6) can be rewritten as follows:

$$x(t) = \Phi_{inj}(t - t_{n2})x_{n2} + A_{inj}^{-1}(\Phi_{inj}(t - t_{n2}) - I)B_{inj}u \quad t_{n2} \leq t_{(n+1)1} \quad (9)$$

Referring to Figure 5, by substituting τ_{osc} and τ_{inj} into Equations (8) and (9), the state variables x_{n1} and x_{n2} at the end of the power injecting state and the oscillating state can be obtained, respectively. x_{n1} and x_{n2} can be derived as follows:

$$\begin{cases} x_{n1} = \Phi_{inj}(\tau_{inj})x_{n2} + A_{inj}^{-1}(\Phi_{inj}(\tau_{inj}) - I)B_{inj}u & t_{n2} \leq t_{(n+1)1} \\ x_{n2} = \Phi_{osc}(\tau_{osc})x_{n1} & t_{n1} \leq t < t_{n2} \end{cases} \quad (10)$$

By combining the two equations in Equation (10), x_{n1} can be expressed as follows:

$$x_{n1} = (I - \Phi_{inj}(\tau_{inj})\Phi_{osc}(\tau_{osc}))^{-1}A_{inj}^{-1}(\Phi_{inj}(\tau_{inj}) - I)B_{inj}u \quad (11)$$

Referring to the vector trajectory shown in Figure 4, if we assume that x has already stabilized at t_{n1} with a value of x_{n1} , then, after a duration of one period T , x will repeatedly return to x_{n1} at $t_{(n+1)1}$. In other words, x_{n1} will be equal to $x_{(n+1)1}$, indicating that x_{n1} is a fixed point. By applying the fixed point mapping calculation, and considering the end-time

point of power injection state t_{n1} , the capacitor voltage of u_p is clamped at U_{DC} . Therefore, the end value of the power injecting stat can be obtained as $C \times x_{n1} = U_{DC}$, where the output matrix $C = [1, 0, 0, 0]$. As a result, Equation (11) can be modified as follows:

$$\begin{cases} U_{DC} = C(I - \Phi_{inj}(\tau_{inj})\Phi_{osc}(\tau_{osc}))^{-1}A_{inj}^{-1}(\Phi_{inj}(\tau_{inj}) - I)B_{inj}U_{DC} \\ C = [1 \quad 0 \quad 0 \quad 0] \end{cases} \quad (12)$$

Taking a power transfer period T as a known variable and Substituting $\tau_{inj} = T - \tau_{osc}$ into Equation (12), Equation (12) can be modified as:

$$\begin{cases} U_{DC} = C(I - \Phi_{inj}(T - \tau_{osc})\Phi_{osc}(\tau_{osc}))^{-1}A_{inj}^{-1}(\Phi_{inj}(T - \tau_{osc}) - I)B_{inj}U_{DC} \\ C = [1 \quad 0 \quad 0 \quad 0] \end{cases} \quad (13)$$

After determining the value of T , the oscillating and injecting durations, τ_{osc} and τ_{inj} , can be obtained by solving Equation (13). The expressions for τ_{osc} and τ_{inj} as functions of T can be written as follows:

$$\begin{cases} \tau_{osc} = f(T) \\ \tau_{inj} = T - f(T) \end{cases} \quad (14)$$

By utilizing Equation (14), the duration of τ_{osc} and τ_{inj} can be calculated. By substituting these calculated results into Equations (10) and (11), the fixed points, x_{n1} and x_{n2} , can be expressed as functions in the following manner:

$$\begin{cases} x_{n1} = F_{inj}(\tau_{osc}, \tau_{inj}) \\ x_{n2} = F_{osc}(\tau_{osc}, x_{n1}) \end{cases} \quad (15)$$

By substituting Equation (15) into Equation (8), the time domain solution of the state variable of the oscillating state can be obtained:

$$x(t) = \Phi_{osc}(t - t_{n1})F_{inj}(\tau_{osc}, \tau_{inj}) \quad t_{n1} \leq t < t_{n2} \quad (16)$$

By substituting Equation (15) into Equation (9), the time domain solution of the state variable of the power injecting state can be obtained:

$$x(t) = \Phi_i(t - t_{n2})F_{osc}(\tau_{osc}, x_{n1}) + A_{inj}^{-1}(\Phi_{inj}(t - t_{n2}) - I)B_{inj}u \quad t_{n2} \leq t_{(n+1)1} \quad (17)$$

According to Equation (3), if we define $C_{up} = [1, 0, 0, 0]$ and $C_{ip} = [0, 1, 0, 0]$, the time domain expression of the voltage u_p and current i_p can be obtained as follows:

$$\begin{cases} u_p(t) = C_{up}\Phi_{osc}(t - t_{n1})F_{inj}(\tau_{osc}, \tau_{inj}) \\ i_p(t) = C_{ip}\Phi_{osc}(t - t_{n1})F_{inj}(\tau_{osc}, \tau_{inj}) \end{cases} \quad t_{n1} \leq t < t_{n2} \quad (18)$$

If we define $C_{uo} = [0, 0, 0, 1]$, the output power can be obtained as follows:

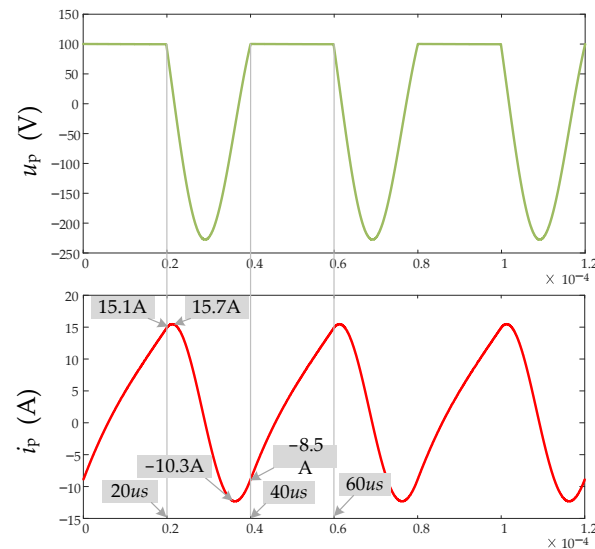
$$P_o = \frac{1}{T} \int_0^T \frac{(C_{uo}\Phi_{osc}(t - t_{n1})F_{inj}(\tau_{osc}, \tau_{inj}))^2}{R_L} dt \quad (19)$$

To verify whether the models in Figures 6 and 7 and the associated theoretical analysis are consistent with Figure 4, as well as to confirm the accuracy of the proposed self-oscillating IPT system, Equations (3)–(18) were simulated and tested using MATLAB R2016b. The parameters used for the validation process are listed in Table 2.

Figure 8 illustrates the calculation results, where the voltage curve u_p and current curve i_p align with Figures 4 and 5, respectively. This confirms the accuracy of the proposed theoretical model. The calculation results indicate that the system enters the oscillating state at 20 μ s, and remains in that state until 40 μ s, resulting in a duration of 20 μ s.

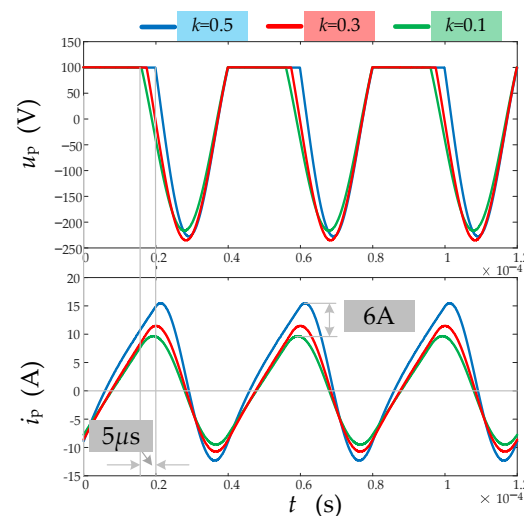
Table 2. The main simulation parameters.

Parameter	Design Value	Parameter	Design Value
UDC	100 V	L_p, L_s	100 μH , 100 μH
M	50 μH	C_p, C_s	0.3 μF , 0.3 μF
R_{ps}, R_{ss}	0.07 Ω , 0.07 Ω	T	40 μs

**Figure 8.** Theoretical calculation results of i_p , u_p .

Subsequently, the system transitions to the power injecting state at 40 μs and exits this state at 60 μs , with a duration of 20 μs . During the onset of the oscillating state, the current value i_p is 15.1 A. Following a 2 μs delay, i_p reaches its maximum value of 15.7 A (I_{pm1}). Similarly, prior to the system exiting the oscillating state, i_p reaches its negative maximum of -10.3 A (I_{pm2}). After a 4 μs delay, when the system exits the oscillating state at 40 μs , i_p measures -8.5 A.

Figure 9 illustrates the impact of the coupling coefficient k on the curves of i_p and u_p with a fixed value of $T = 40$ μs . As depicted in the figure, with k varying from 0.5 to 0.1, the starting time of the oscillating state advances by approximately 5 μs , while the amplitude of i_p decreases by approximately 6 A. For a more detailed analysis of the effect of k on the oscillating state duration, τ_{osc} , and the amplitude, I_{pm1} , please refer to Figure 10.

**Figure 9.** The influence of parameters on self-oscillation.

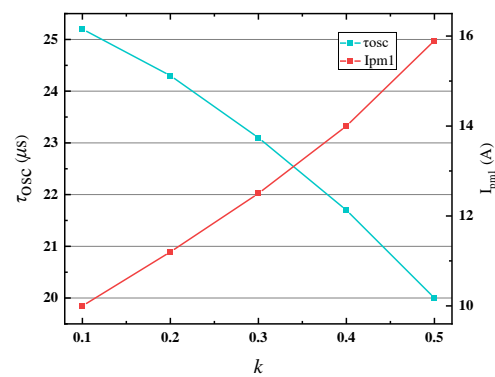


Figure 10. The relationship between coupling coefficient k , self-oscillating state duration τ_{osc} , and amplitude of i_p .

For a more detailed analysis of the effect of coupling coefficient k on the duration of the oscillating state, τ_{osc} , and the amplitude of the primary current i_p , I_{pm1} , Figure 10 illustrates the relationship between τ_{osc} and I_{pm1} as a function of k . The figure demonstrates that the τ_{osc} decreases with increasing values of k . This is attributed to the fact that a higher coupling coefficient results in a smaller leakage inductance L_{pk} for the loosely coupled transformer, consequently leading to a shorter oscillation period. Furthermore, it should be noted that an increase in the coupling coefficient also corresponds to an amplified amplitude of the primary current i_p . This can be attributed to the enhanced power transmission to the secondary side as k increases. Therefore, on the primary side, a greater amount of power needs to be injected during the power injecting state duration.

Clearly, the calculated results of Figures 9 and 10 precisely correspond to those of Figures 4 and 5, providing further evidence of the accuracy of the proposed theoretical models.

4. Control Method

As analyzed in Section 2, achieving oscillation phase tracing and power injection duration control are the key objectives of the proposed IPT system. Therefore, this chapter focuses on the methods employed to fulfill these requirements. Figure 11 illustrates the circuit diagram of the dynamic IPT system studied in this paper.

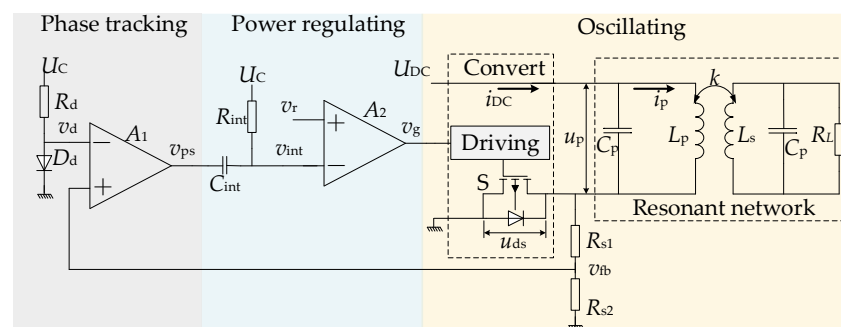


Figure 11. The circuit diagram of the proposed dynamic IPT system.

In this IPT system, a closed-loop phase tracking circuit is utilized to track the phase and trigger self-oscillation. This self-oscillating circuit consists of three components: phase tracking unit, power regulating unit, and oscillating unit. With this closed-loop control, the system achieves self-oscillation.

4.1. The Oscillating Unit

The oscillating unit adopts a topology that includes a single switch converter and an oscillating network. The converter employs an IGBT as switch S , while the oscillating network consists of the primary capacitor C_p , and inductor L_p . As depicted in Figure 1,

the oscillation unit can alternate between the oscillating state and the power injecting state by controlling the switch S. To acquire the phase information of the system oscillation, a voltage divider comprising R_{s1} and R_{s2} is utilized as a sensor to monitor the voltage across switch S, denoted as u_{ds} . The expression for u_{ds} is:

$$u_{ds} = (U_{DC} - u_p) \quad (20)$$

The output of the sensor, v_{fb} , can be calculated using the following formula:

$$v_{fb} = \frac{R_{s2}}{R_{s1} + R_{s2}} u_{ds} \quad (21)$$

4.2. Phase Tracking Unit

The phase tracking unit comprises R_d , D_d and comparator A_1 , which is employed for tracking phase changes. R_d and D_d are responsible for generating a comparison threshold voltage v_d of 0.7 V, which is applied to the negative terminal of A_1 . The feedback signal v_{fb} is then fed to the positive terminal of A_1 and compared with v_d . The output of A_1 , v_{ps} , can be expressed as follows:

$$v_{ps} = \begin{cases} 0 & v_{fb} < v_d \\ U_C & v_{fb} > v_d \end{cases} \quad (22)$$

Based on Figure 4, and Equation (21), the signal v_{fb} is a sinusoidal pulse sequence in which pulse width signifies the duration of the oscillating state, τ_{osc} (phase angle $\beta_{\tau 2}$). Consequently, the duration of the high level output of v_{ps} , aligns with the duration of the oscillation state, τ_{osc} . Notably, according to Equation (22), the high-level duration of v_{ps} can be automatically adjusted to track τ_{osc} (phase angle $\beta_{\tau 2}$), thereby facilitating the phase tracking within the system.

A phase tracking process can be demonstrated using Figure 12. In the figure, the curves before the phase change are highlighted in green, while the curves after the phase change are marked in red. Suppose a phase shift occurs due to some reason, this results in a change in the width of v_{fb} from τ_{osc} to τ_{osc}' as the phase transitions from $\beta_{\tau 2}$ to $\beta_{\tau 2}'$. By comparing it with the threshold v_d , the width of v_{ps} also tracks this change, shifting from τ_{osc} to τ_{osc}' . As shown in Figure 12, this method enables the system to promptly track the phase shift.

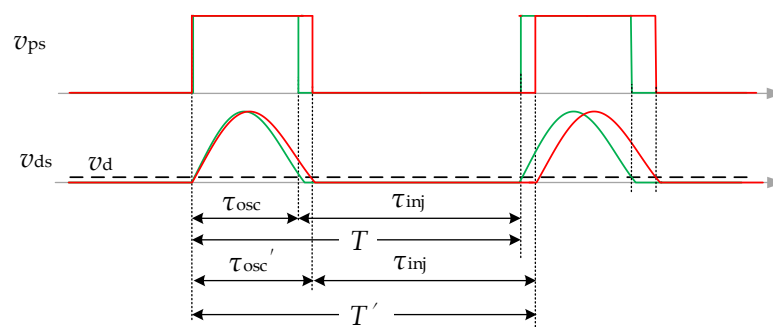


Figure 12. Phase tracking schematic diagram.

4.3. Power Injecting Unit

The power regulating unit comprises a comparator A_2 and an integrator. The integrator is composed of a resistor R_{int} and capacitor C_{int} . The control signal, v_{ps} , is connected to the input of the integrator, as depicted in Figure 13. This configuration demonstrates how the integrator operates under the control of output of comparator A_1 , v_{ps} . To simplify the analysis, the output of A_1 is considered equivalent to a transistor push–pull structure.

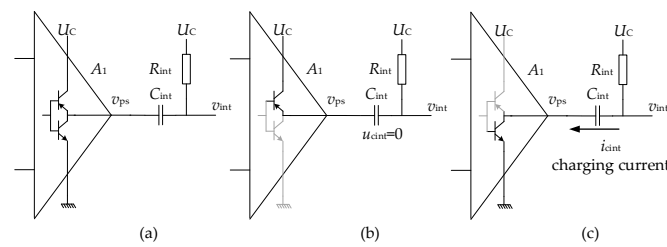


Figure 13. Schematic diagram of integrator operation. (a) Integrator stop state. (b) Integrator push-up state. (c) Integrator pull-down state.

Referring to Figure 13, the control process of v_{ps} for the integrator can be described as follows:

- (1) When v_{ps} is at a high level, the upper switch of the push-pull structure is turned on, as depicted in Figure 13b. In this case, both ends of the capacitor C_{int} are connected to U_C , resulting in zero voltage across C_{int} . Consequently, the integrator ceases its operation, and the integrator output $v_{int} = U_C$.
- (2) As v_{ps} is lowered, the lower switch of the push-pull structure is activated, as shown in Figure 13c. In this scenario, the input of the integrator is connected to the ground, initiating the charging of capacitor C_{int} through R_{int} by U_C . As a result, the output of the integrator, v_{int} , begins to increase from zero. The expression for v_{int} can be represented as follows:

$$v_{int} = \frac{1}{C_{int}} \int_{t_0}^t \frac{U_C}{R_{int}} dt \quad (23)$$

In Equation (23), t_0 represents the time at which the integrator begins its operation. Assuming that the moment v_{ps} is pulled to low level corresponds to the time when the integrator starts working, then t_0 can be set to 0. In this case, v_{int} can be expressed as follows:

$$v_{int} = \frac{1}{C_{int}} \int_0^t \frac{U_C}{R_{int}} dt = \frac{U_C}{R_{int} C_{int}} t \quad (24)$$

The output of the integrator, v_{int} , is then compared with a threshold v_r in comparator A_2 , and the comparison result v_g can be expressed as follows:

$$v_g = \begin{cases} U_C & v_{int} < v_r \\ 0 & v_{int} > v_r \end{cases} \quad (25)$$

The control signal v_g is sent to the oscillating unit to control the switch S, turning it on or off. It is evident that by controlling the duration of v_g at the high level, the output power of the system can be regulated. Since v_{int} is a signal that starts at zero and rises linearly, according to Equation (25), the duration of v_g is determined by the threshold v_r . Hence, v_r can be used as a variable to control the system power.

Figure 14 illustrates the principle of utilizing v_r to control the system power. In the figure, the green and red lines represent the waveforms before and after the change in v_r , respectively. Figure 14 demonstrates that when the power control variable is increased from v_r to v_r' , the end time of power injecting state extends from $t_{(n+1)1}$ to $t_{(n+1)1}'$, and the duration of power injecting extends from τ_{inj} to τ_{inj}' .

As depicted in Figure 14, with the increase in τ_{inj} , the amplitudes of i_p also increase from I_{pm1} and I_{pm2} to I_{pm1}' and I_{pm2}' , respectively, indicating an increase in the power injected into the system. Conversely, if v_r is decreased, the power injected into the system will be reduced accordingly.

Hereto, the challenges to tracking the oscillation phase and controlling the duration of power injection have been successfully resolved. To provide a clearer representation,

Figure 11 is depicted as a block diagram in Figure 15, illustrating the operational process of the proposed IPT system.

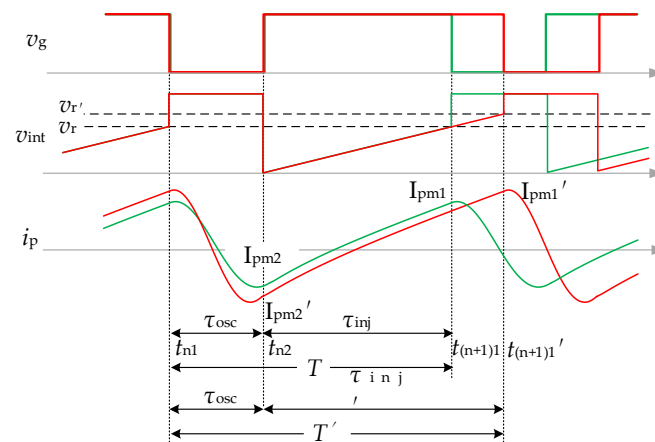


Figure 14. The principle of power regulation.

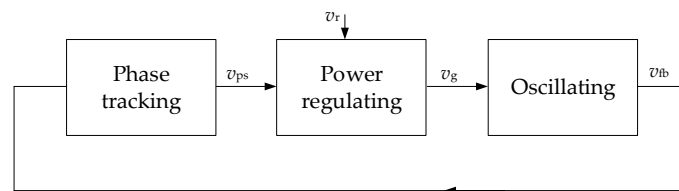


Figure 15. Self-oscillating closed loop block diagram based on Phase Tracking.

Initially, the signal v_{fb} , which carries the oscillating network information, is directed to the phase tracking unit. This unit detects the duration of the oscillating state, τ_{osc} , and generates the output signal v_{ps} .

Subsequently, v_{ps} serves as a trigger signal to initiate the power regulating unit. By utilizing the control variable v_r , the power regulating unit determines the duration of the power injecting state, τ_{inj} , and generates the control signal v_g .

Ultimately, the control signal v_g is transmitted to the oscillating unit, which seamlessly transitions between the self-oscillating state and the power injecting state, thereby completing the self-oscillating closed loop of the system.

Figure 16 presents the curves of crucial signals during each operation of the proposed IPT system, elucidating the temporal relationship between these signals. This visualization aims to enhance comprehension of the system's working principle.

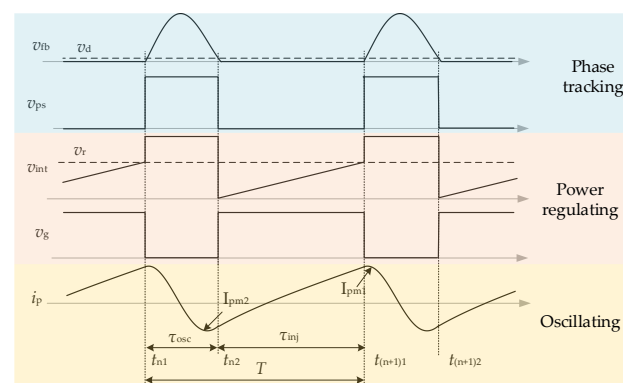


Figure 16. The curves of the proposed IPT system.

5. Validate Prototypes and Experiment

A verification platform was built to verify the theoretical analysis of the proposed dynamic IPT system, as shown in Figure 17, which includes a prototype made according to Figure 11. In the experimental platform, an oscilloscope (ROHDE&SCHWARZ RTB2004, Munich, Germany) and a power analyzer (YOKOGAWA WT500, Tokyo, Japan) are hired to monitor the working waveform and analyze the system power, respectively. A resistance group consisting of four resistors and switches is used to provide different load resistor. In the experiment, the main parameters of the experimental platform are listed in Table 3, and L_p , L_s , C_p , C_s can be obtained from Table 2.

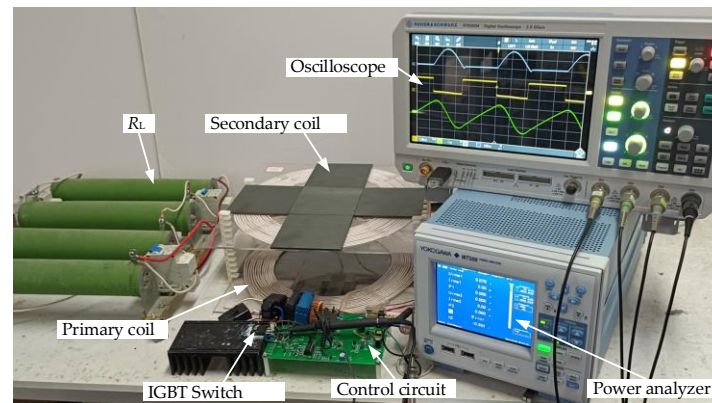


Figure 17. The verification prototype of the proposed dynamic IPT system.

Table 3. The main parameters of the verify prototype.

Parameter	Value	Parameter	Value
U_{DC}, U_c	100–200 V, 5 V	Comparator	LM339
R_{int}, C_{int}	50 k, 20 nF	R_d, D_d	1 k, 1N4148
IGBT	H30R1602	R_L	10–50 Ω

The primary and secondary coils used in the experimental platform are made of a 3 mm diameter Leeds wire wound 18 turns, and a cross-shaped ferrite core was installed behind the coil. Both the coils are tested by a digital electric bridge (VICTOR 4091C LCR, Shenzhen, China). According to the test results, the relationship of the coupling coefficient k between the coils and the air gap d can be obtained, as shown in Figure 18.

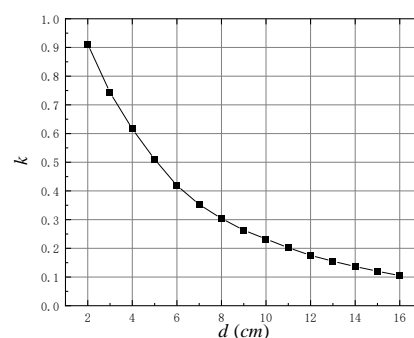


Figure 18. The relationship between the coil coupling coefficient and air gap.

5.1. Self-Oscillation Characteristic Verification

The curves of i_p , i_{cp} , i_{DC} , and v_{ds} were obtained from the experiment, as depicted in Figure 19. Here, v_{ds} represents the voltage across switch S , given by Equation (20), where it is used to represent u_p . The following phenomena can be observed in this experiment:

- (1) The system operates in a closed loop, following the sequence of the blocking (self-oscillating) state, τ_2 , the diode-on state τ_3 , and the switch-on state τ_1 , as described in Figure 4. This demonstrates that the system is capable of self-oscillation, with the oscillation process repeating in the oscillating state, τ_{osc} , and the power injecting state, τ_{inj} .
- (2) During the oscillating state, i_{DC} is equal to zero, indicating that the oscillating network is isolated from U_{DC} . The capacitor C_p and inductor L_p form a resonant tank and initiate oscillation. The capacitor voltage, v_{ds} (u_p), capacitor current, i_{cp} , and the inductor current, i_p , exhibit sinusoidal changes, with i_{cp} and i_p being equal. Clearly, the oscillation is sustained for less than one cycle. The oscillation state duration τ_{osc} being 22 μs , slightly larger than the simulation results shown in Figure 8. This deviation may be caused by the deviation of component parameters.
- (3) In the diode-on state, i_{DC} is negative, indicating that the current i_p flows back to U_{DC} through the diode. In the switch-on state, i_{DC} is positive, indicating that U_{DC} injects a current into the inductor L_p . Combining the diode-on state, τ_3 , and the switch-on state, τ_1 , into the power injecting state τ_{inj} , it can be observed that during the power injecting state, i_p linearly increases from negative to positive with a rise slope of 1×10^6 A/s, consistent with the calculated result from Equation (1). Additionally, the capacitor current, i_{cp} , is zero during the power injecting state, implying that the capacitor voltage is clamped to U_{DC} during these two states.

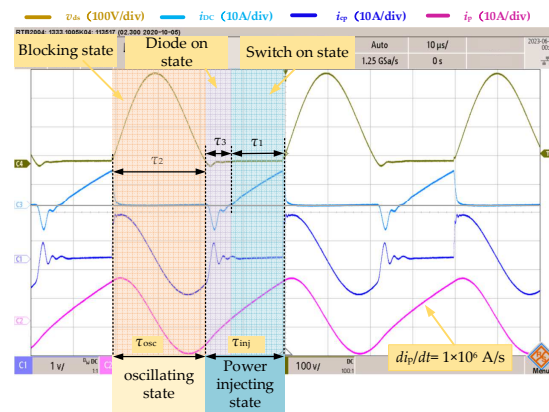


Figure 19. The curves of i_p , i_{cp} , i_{DC} , and v_{ds} , under $U_{DC} = 100$ V, $d = 5$ cm, $R_L = 10 \Omega$.

This experimental results are consistent with the theoretical analysis presented in Figures 1 and 4. Additionally, the experimental results closely correspond to the simulation result depicted in Figure 8, thus validating the accuracy of the model established in Section 3.

5.2. Power Regulating Verification

Figure 20 exhibits the experimental curves of u_{ds} , v_g , v_{int} and i_p , serving as a means to assess the performance of the IPT system outlined in Figure 11, as well as the impact of the control variable v_r on the system's output power regulation. Specifically, in subfigure (a), with v_r set to 2.5 V, and in subfigure (b), with v_r set to 3.5 V. The experimental results yield the following observations:

- (1) The experimental curves are exactly the same as the principle curves shown in Figure 16, which indicates that the system can realize self-oscillation according to the order of the self-oscillating state and power injecting state.
- (2) The power injecting state duration can only be controlled by the control variable v_r . The comparison between (a) and (b) shows that when v_r increases from 2.5 V to 3.5 V, the power injection duration τ_{inj} increases from 24 μs to 36 μs , and the amplitude I_{pm1} of the current i_p increases from 14 A to 20 A, indicating that the power can be adjusted by controlling v_r .

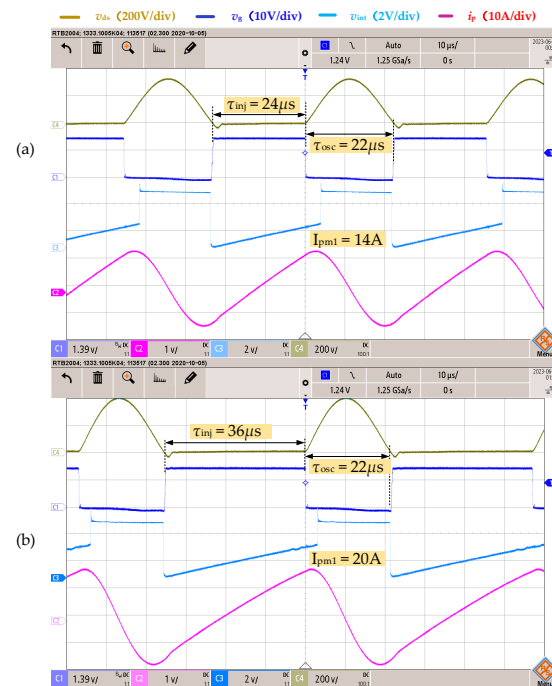


Figure 20. The performance experimental, under $U_{DC} = 100$ V, $d = 5$ cm, $R_L = 10$ Ω . (a) With v_r set to 2.5 V. (b) With v_r set to 3.5 V.

It is noted that when the control variable v_r adjusts the power injecting state duration, the self-oscillating state duration τ_{osc} is not affected and is maintained at 22 μ s. This shows that the power injection process is decoupled from the self-oscillation process.

Figure 21 illustrates the relationship between output power, efficiency, and the control variable v_r . This experimental result demonstrates a monotone positive correlation between output power and v_r . The reason for this correlation is that the proposed IPT system's power injection process is decoupled from the self-oscillation process. The power is solely regulated by the control variable v_r . This characteristic simplifies the design of output power regulation and provides a convenient technical implementation for voltage, current, or power closed-loop control within the system.

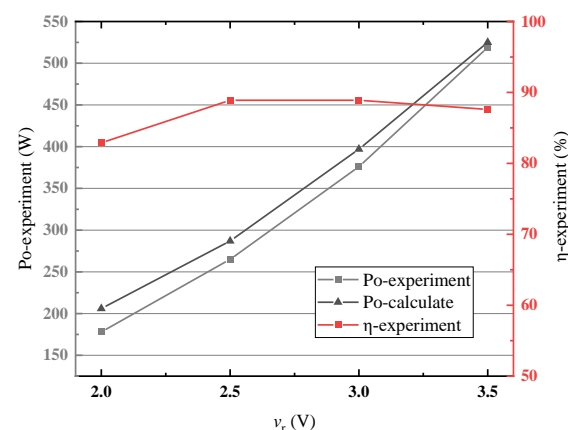


Figure 21. Power and efficiency vs. the control variable v_r , under $U_{DC} = 200$ V, $d = 5$ cm, $R_L = 10$ Ω .

There is a discrepancy between the calculated output power value and the experimental value shown in Figure 21. This deviation occurs because the phase tracking unit employs the forward voltage v_d of diode D, 0.7 V, as a threshold, as illustrated in Figure 16. Consequently, the detected value of the self-oscillation state duration is smaller than the actual value, resulting in the experimental output power value being lower than the value

calculated using Equation (19). Nevertheless, as the output power increases, the influence of the self-oscillating state duration diminishes, bringing the experimental output power value closer to the calculated value.

It can be observed that in Figure 21, the efficiency at $v_r = 2.5$ V and 3.0 V reaches an optimal value of 89.2%, while it decreases to 83.5% and 87.6% at $v_r = 2$ V and 3.5 V, respectively. This phenomenon occurs because the power is regulated by adjusting the transmission period, which can lead the system to deviate from the optimal equivalent impedance.

5.3. Phase Tracking and Soft Switch Condition Verification

Figure 22 illustrates the experimental curves of i_p , u_{ds} and the control signal v_g of switch S, providing evidence of the phase tracking characteristic of the proposed IPT system. The results reveal that when $d = 3$ cm, the self-oscillating state lasts for $\tau_{osc} = 22.1 \mu s$, and the power injecting state persists for $\tau_{inj} = 17.8 \mu s$. With an increase in $d = 12$ cm, the duration of the self-oscillating state extends to $26.3 \mu s$, while the power injecting state remains unchanged at $\tau_{inj} = 17.8 \mu s$.

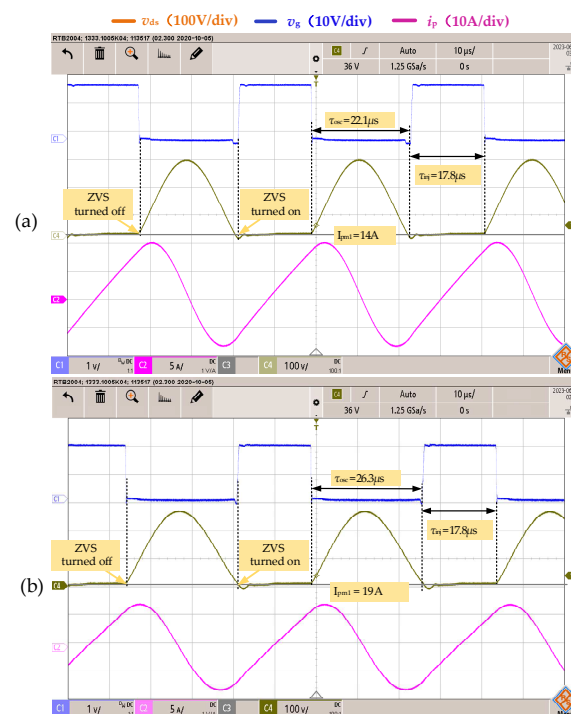


Figure 22. The experimental of phase tracking characteristic, under $U_{DC} = 100$ V, $R_L = 10 \Omega$, (a) $d = 3$ cm, (b) $d = 12$ cm.

This experiment clearly demonstrates the system's excellent good phase (frequency) tracking capability and confirms that the self-oscillation method proposed in this paper does not interfere with each other between the self-oscillating state and the power injecting state. Significantly, it can be observed that, despite the variation in the self-oscillating state duration, the switch S effectively tracks the change and remains at the ZVS soft switching point.

5.4. Dynamic Characteristics Verification

To test the dynamic characteristics and robustness of the system, an experiment was conducted involving the shifting of the coil's position. The procedure for the experiment is as follows: initially, the secondary coil was positioned more than 20 cm away from the primary coil. Subsequently, the secondary coil was rapidly moved to a position just 3 cm away from the primary coil. The experimental results are represented by the curves of v_g and i_p , which were captured by the oscilloscope and depicted in Figure 23.

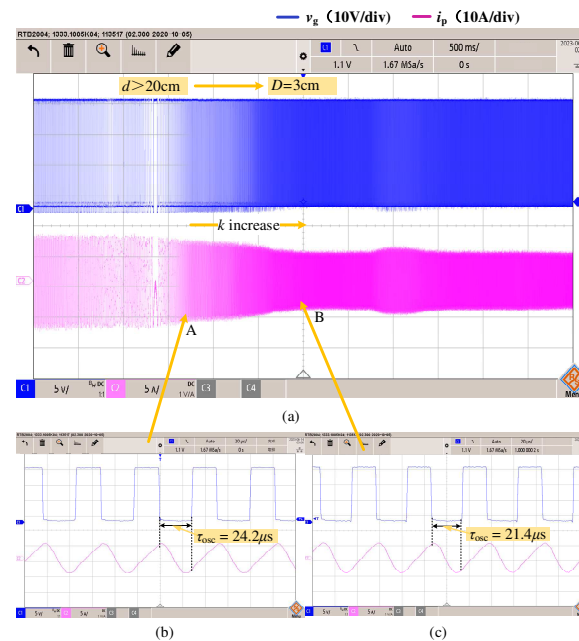


Figure 23. The experiment for dynamic characteristics and robustness of the system. (a) Experimental curves of air gap change from 20 cm to 3 cm at a scale of 500 ms/div. (b) The curve unfolded at a scale of 20 μs /div at point A. (c) The curve unfolded at a scale of 20 μs /div at point B.

Figure 23a illustrates the curves obtained at a scale of 500 ms/div, which is used to depict the overall dynamic process in the experiment. On the other hand, (b,c) display the curves unfolded at a scale of 20 μs /div, captured at different time points from (a), aiming to present detailed information in dynamic experiments. The experimental results demonstrate that the system can accurately track the phase change caused by the alteration of coupling coefficient. Throughout the experiment, as the coil distance varies, the duration of the oscillating state automatically adjusts from 24.2 μs to 21.4 μs .

Furthermore, an experiment on sudden load tolerance was conducted. In this experiment, the load steps from 10 Ω to 30 Ω , and then returned to 20 Ω . Figure 24a depicts the experimental results obtained at a scale of 500 ms/div, demonstrating that all the curves effectively track the changes in load.

Figure 24b provides an expanded of Figure 24a at time point t_{s1} , offering a detailed examination of the transition from 10 Ω to 30 Ω . The revealed details indicate that the curve transition remarkably smooth, taking only 10 cycles to complete.

Moving on to Figure 24c,d, it further amplifies the data from Figure 24b, this time at a scale of 20 μs /div. Specifically, Figure 24c focuses on the $R_L = 10\text{ }\Omega$ scenario, while Figure 24d looks at $R_L = 30\text{ }\Omega$. Notably, the power injection time remaining at the self-oscillation time increases from 21.4 μs to 23.6 μs . This outcome suggests that the load change solely impacts the resonant angular frequency of the self-oscillation, highlighting the decoupling of the power injection process from the self-oscillation process.

These experimental findings substantiate the effectiveness of the proposed closed loop self-oscillating structure, which exhibits the ability to track parameter changes in one period while showcasing remarkable robustness of the system.

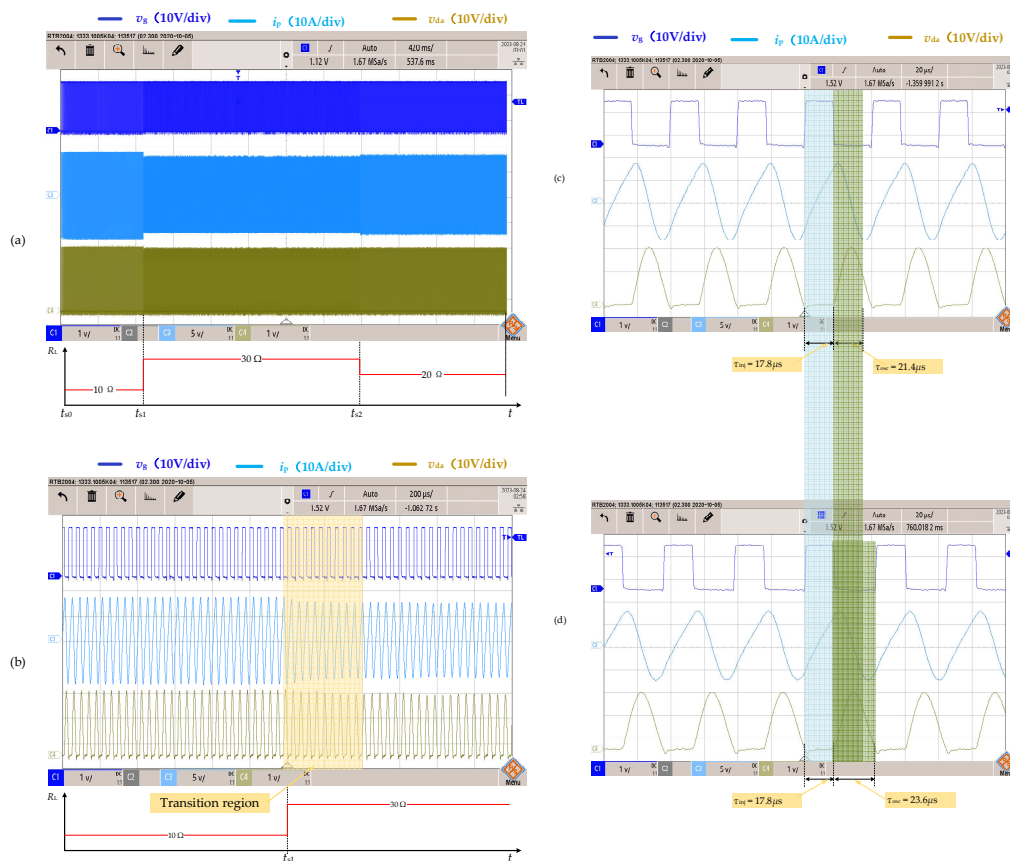


Figure 24. Experiment of dynamic characteristics under step change of load. (a) The curve that depicts the experimental results obtained at a scale of 500 ms/div. (b) The curve that provides an expanded of Figure 24a at time point t_{s1} , offering a detailed examination of the transition from 10 Ω to 30 Ω . (c,d) The curve that further amplifies the data from (b), this time at a scale of 20 μs /div. Specifically, (c) focuses on the $R_L = 10 \Omega$ scenario, while (d) looks at $R_L = 30 \Omega$.

6. Conclusions

To address the challenges associated with frequency tracking and power control in conventional IPT system, which arise due to the coupling between the converter and the resonant network, this study proposes a method for implementing an IPT system based on a phase-closed loop. This method divides a power transfer process into two distinct states: the self-oscillating state and power injecting state, and ensures their independence from each other. The effectiveness of this method was verified through simulation and experiments, which led to the following conclusions:

- (1) The working process of a converter can be divided into three distinct states: the switch-on state, blocking state, and diode-on state. This division allows for decoupling of the resonant network from the converter. By combining the switch-on state and diode-on state into power injecting state, and considering the blocking state as oscillating state, the working process of an IPT system consists of two state sequences: power injecting and oscillating states. By controlling the duration of the power injecting state, the output power can be adjusted independently. Furthermore, by detecting the duration of the self-oscillating state, changes in frequency can be accurately tracked and compensated for. The diode-on state's soft switching characteristics enable a smooth transition between the power injecting and oscillating states.
- (2) The proposed phase-closed loop, comprising the phase tracking unit, power regulating unit, and oscillating unit, proves to be effective. This closed loop enables the system to switch between the power injecting state and oscillating state under soft switching condition.

- (3) Experimental results demonstrate that the phase tracking unit accurately tracks frequency drift caused by system parameters, indicating excellent frequency tracking characteristics. Furthermore, the experiments show that the system exhibits robust frequency tracking, even under conditions of a large coupling coefficient and maximum speed change.
- (4) The proposed power control method utilizing an integrator is proved to be effective. With the power injecting process decoupling from the oscillating process, power regulation only requires manipulation of the control variable v_r . The experimental results indicate that the output power monotonically increases with the control variables v_r . This power regulation characteristic simplifies and enhances the reliability of designing an IPT system control strategy.

Author Contributions: Conceptualization, W.C. and L.C.; methodology, W.C. and L.C.; software, J.H. and M.G.; validation, W.C. and L.C.; formal analysis, W.C. and L.C.; investigation, D.L.; resources, W.C.; data curation, L.C.; writing—original draft preparation, W.C. and D.L.; writing—review and editing, J.H., M.G. and D.L.; visualization, W.C. and L.C.; supervision, W.C.; project administration, W.C.; funding acquisition, W.C. and J.H. All authors have read and agreed to the published version of the manuscript.

Funding: This research was funded by Natural Science Foundation of Fujian Province, grant number 2021J05262 and 2021J011202, Fujian Provincial Science and Technology Plan Project, grant number 2022T3061, and National Natural Science Foundation of China, grant number 52177222.

Data Availability Statement: The authors confirm that the data supporting the findings of this study are available within the article.

Conflicts of Interest: The authors declare no conflicts of interest.

Nomenclature

IPT	Inductive Power Transfer
ZPA	Zero Phase Angle
PLL	Phase-Locked Loop
ZVS	Zero Voltage Switch
U_{DC}	Bus-bar voltage
L_p	Primary inductance
L_s	Secondary inductance
L_{pk}	Primary leakage inductance
L_{sk}	Secondary leakage inductance
M	Mutual inductance
L_M	mutual inductance
k	Coupling coefficient
K_E	Primary current slop
C_p	Primary capacitance
C_s	Secondary capacitance
C_{int}	Integrating capacitance of power injecting unit
R_L	Equivalent load
R_{ps}	Primary loss resistance
R_{ss}	Secondary loss resistance
R_{int}	Integrating resistance of power injecting unit
A_1	Phase tracking unit comparator
A_2	Power regulating unit comparator
S	Power switch
i_p	Primary inductor current
i_s	Secondary inductor current

u_p	Primary capacitor voltage
u_o	Output voltage
u_{ds}	Voltage across switch S
v_g	Control signal of switch
v_{fb}	Feedback signals from the oscillating network
v_d	Comparison threshold of Phase tracking unit
v_{ps}	Output voltage of Phase tracking unit
v_{int}	Integrator output voltage
v_r	System power control voltage
τ_1	Duration of switch-on state
τ_2	Duration of blocking state
τ_3	Duration of diode-on state
τ_{inj}	Duration of power injecting state
τ_{osc}	Duration of self-oscillating state
ω	Self-oscillating angular frequency
$\beta_{\tau 1}$	Phase angle occupied by switch-on state
$\beta_{\tau 2}$	Phase angle occupied by blocking state
$\beta_{\tau 3}$	Phase angle occupied by diode-on state
P_0	Output power
I_{pm1}/I_{pm2}	Maximum value of primary current, i_p
T	Energy transfer period
d	The air gap between the two coils
I_{dc}	Bus current

References

- Liu, H.; Shao, Q.; Fang, X. Modeling and Optimization of Class-E Amplifier at Subnominal Condition in a Wireless Power Transfer System for Biomedical Implants. *IEEE Trans. Biomed. Circuits Syst.* **2016**, *11*, 35–43. [\[CrossRef\]](#)
- Ruffo, R.; Cirimele, V.; Diana, M.; Khalilian, M.; La Ganga, A.; Guglielmi, P. Sensorless control of the charging process of a dynamic inductive power transfer system with interleaved nine-phase boost converter. *IEEE Trans. Ind. Electron.* **2018**, *65*, 7630–7639. [\[CrossRef\]](#)
- Zhao, L.; Thrimawithana, D.J.; Madawala, U.K.; Hu, A.P. A Push–Pull Parallel Resonant Converter-Based Bidirectional IPT System. *IEEE Trans. Power Electron.* **2019**, *35*, 2659–2667. [\[CrossRef\]](#)
- Wang, C.S.; Covic, G.A.; Stielau, O.H. Investigating an LCL load resonant inverter for inductive power transfer applications. *IEEE Trans. Power Electron.* **2004**, *19*, 995–1002. [\[CrossRef\]](#)
- Zhang, W.; Wong, S.-C.; Tse, C.K.; Chen, Q. Design for Efficiency Optimization and Voltage Controllability of Series–Series Compensated Inductive Power Transfer Systems. *IEEE Trans. Power Electron.* **2013**, *29*, 191–200. [\[CrossRef\]](#)
- Stielau, O.H.; Covic, G.A. Design of loosely coupled inductive power transfer systems. In Proceedings of the 2000 International Conference on Power System Technology, Perth, WA, Australia, 4–7 December 2000. [\[CrossRef\]](#)
- Mohamed, A.A.S.; Berzoy, A.; de Almeida, F.G.N.; Mohammed, O. Modeling and Assessment Analysis of Various Compensation Topologies in Bidirectional IWPT System for EV Applications. *IEEE Trans. Ind. Appl.* **2017**, *53*, 4973–4984. [\[CrossRef\]](#)
- Shevchenko, V.; Husev, O.; Strzelecki, R.; Pakhaliuk, B.; Poliakov, N.; Strzelecka, N. Compensation Topologies in IPT Systems: Standards, Requirements, Classification, Analysis, Comparison and Application. *IEEE Access* **2021**, *7*, 120559–120580. [\[CrossRef\]](#)
- Houran, M.A.; Yang, X.; Chen, W. Magnetically Coupled Resonance WPT: Review of Compensation Topologies, Resonator Structures with Misalignment, and EMI Diagnostics. *Electronics* **2018**, *7*, 296. [\[CrossRef\]](#)
- Mohamed, A.A.S.; Shaier, A.A.; Metwally, H.; Selem, S.I. An Overview of Dynamic Inductive Charging for Electric Vehicles. *Energies* **2022**, *15*, 5613. [\[CrossRef\]](#)
- Wang, C.S.; Covic, G.A.; Stielau, O.H. Power transfer capability and bifurcation phenomena of loosely coupled inductive power transfer systems. *IEEE Trans. Ind. Electron.* **2004**, *51*, 148–157. [\[CrossRef\]](#)
- Villa, J.L.; Sallan, J.; Osorio, J.F.S.; Llombart, A. High-Misalignment Tolerant Compensation Topology for ICPT Systems. *IEEE Trans. Ind. Electron.* **2011**, *59*, 945–951. [\[CrossRef\]](#)
- Fotopoulou, K.; Flynn, B.W. Wireless Power Transfer in Loosely Coupled Links: Coil Misalignment Model. *IEEE Trans. Magn.* **2011**, *47*, 416–430. [\[CrossRef\]](#)
- Su, Y.-G.; Zhang, H.-Y.; Wang, Z.-H.; Hu, A.P.; Chen, L.; Sun, Y. Steady-State Load Identification Method of Inductive Power Transfer System Based on Switching Capacitors. *IEEE Trans. Power Electron.* **2015**, *30*, 6349–6355. [\[CrossRef\]](#)
- Li, Y.; Dong, W.; Yang, Q.; Jiang, S.; Ni, X.; Liu, J. Automatic Impedance Matching Method with Adaptive Network Based Fuzzy Inference System for WPT. *IEEE Trans. Ind. Inform.* **2020**, *16*, 1076–1085. [\[CrossRef\]](#)
- Luo, Y.; Yang, Y.; Chen, S.; Wen, X. A Frequency-Tracking and Impedance-Matching Combined System for Robust Wireless Power Transfer. *Int. J. Antennas Propag.* **2017**, *2017*, 5719835. [\[CrossRef\]](#)

17. Zahiribarsari, V.; Thrimawithana, D.J.; Covic, G.A. An Inductive Coupler Array for In-Motion Wireless Charging of Electric Vehicles. *IEEE Trans. Power Electron.* **2021**, *36*, 9854–9863.
18. Gati, E.; Kampitsis, G.; Manias, S. Variable Frequency Controller for Inductive Power Transfer in Dynamic Conditions. *IEEE Trans. Power Electron.* **2016**, *32*, 1684–1696. [[CrossRef](#)]
19. Matysik, J.T. The Current and Voltage Phase Shift Regulation in Resonant Converters with Integration Control. *IEEE Trans. Ind. Electron.* **2007**, *54*, 1240–1242. [[CrossRef](#)]
20. Kim, D.H.; Kim, M.S.; Kim, H.J. Frequency-Tracking Algorithm Based on SOGI-FLL for Wireless Power Transfer System to Operate ZPA Region. *Electronics* **2020**, *9*, 1303. [[CrossRef](#)]
21. Hong, J.; Guan, M.; Lin, Z.; Fang, Q.; Wu, W.; Chen, W. Series-Series/Series Compensated Inductive Power Transmission System with Symmetrical Half-Bridge Resonant Converter: Design, Analysis, and Experimental Assessment. *Energies* **2019**, *12*, 2268. [[CrossRef](#)]
22. Namadmalan, A. Self-Oscillating Tuning Loops for Series Resonant Inductive Power Transfer Systems. *IEEE Trans. Power Electron.* **2016**, *31*, 7320–7327. [[CrossRef](#)]
23. Xu, L.; Chen, Q.; Ren, X.; Wong, S.; Tse, C. Self-Oscillating Resonant Converter with Contactless Power Transfer and Integrated Current Sensing Transformer. *IEEE Trans. Power Electron.* **2016**, *32*, 4839–4851. [[CrossRef](#)]
24. Namadmalan, A. Self-Oscillating Pulse Width Modulation for Inductive Power Transfer Systems. *IEEE J. Emerg. Sel. Top. Power Electron.* **2019**, *8*, 1813–1820. [[CrossRef](#)]
25. Wei, Z.; Zhang, B.; Lin, S.; Wang, C. A Self-Oscillation WPT System with High Misalignment Tolerance. *IEEE Trans. Power Electron.* **2023**, *39*, 1870–1887. [[CrossRef](#)]
26. Li, H.; Li, J.; Wang, K.; Chen, W.; Yang, X. A Maximum Efficiency Point Tracking Control Scheme for Wireless Power Transfer Systems Using Magnetic Resonant Coupling. *IEEE Trans. Power Electron.* **2015**, *30*, 3998–4008. [[CrossRef](#)]
27. Miller, J.M.; Onar, O.C.; Chinthavali, M. Primary-Side Power Flow Control of Wireless Power Transfer for Electric Vehicle Charging. *IEEE J. Emerg. Sel. Top. Power Electron.* **2014**, *3*, 147–162. [[CrossRef](#)]
28. Hu, H.; Cai, T.; Duan, S.; Zhang, X.; Niu, J.; Feng, H. An Optimal Variable Frequency Phase Shift Control Strategy for ZVS Operation within Wide Power Range in IPT Systems. *IEEE Trans. Power Electron.* **2019**, *35*, 5517–5530. [[CrossRef](#)]
29. Berger, A.; Agostinelli, M.; Vesti, S.; Oliver, J.A.; Cobos, J.A.; Huemer, M. A Wireless Charging System Applying Phase-Shift and Amplitude Control to Maximize Efficiency and Extractable Power. *IEEE Trans. Power Electron.* **2015**, *30*, 6338–6348. [[CrossRef](#)]
30. Wu, W.; Luo, D.; Hong, J.; Tang, Z.; Chen, W. A Six-Switch Mode Decoupled Wireless Power Transfer System with Dynamic Parameter Self-Adaption. *Electronics* **2023**, *12*, 2314. [[CrossRef](#)]
31. Chen, L.; Hong, J.; Lin, Z.; Luo, D.; Guan, M.; Chen, W. A Converter with Automatic Stage Transition Control for Inductive Power Transfer. *Energies* **2020**, *13*, 5268. [[CrossRef](#)]
32. Dranga, O.; Buti, B.; Nagy, I.; Funato, H. Stability analysis of nonlinear power electronic systems utilizing periodicity and introducing auxiliary state vector. *IEEE Trans. Circuits Syst. I Regul. Pap.* **2005**, *52*, 168–178. [[CrossRef](#)]
33. Buti, B.; Nagy, I.; Ohsaki, H.; Masada, E. Novel Approach in Stability Analysis Presented in Controlled Boost Converter. In *Proceedings of the Power Conversion Conference, Nagoya, Japan, 2–5 April 2007*; IEEE: Piscataway, NJ, USA, 2007; pp. 581–587.

Disclaimer/Publisher’s Note: The statements, opinions and data contained in all publications are solely those of the individual author(s) and contributor(s) and not of MDPI and/or the editor(s). MDPI and/or the editor(s) disclaim responsibility for any injury to people or property resulting from any ideas, methods, instructions or products referred to in the content.